Spatio-temporal dynamics of macroglial cell organisation and proximity to blood vessels during postnatal development

Running title: Develomental macroglia organisation

Naomie Guille[1], Héloïse Monnet[1], Tristan Hourcade[1], Philippe Mailly[1], Martine Cohen-Salmon[1] and Anne-Cécile Boulay[1]

Center for Interdisciplinary Research in Biology (CIRB), Collège de France, CNRS, INSERM, Université Paris Sciences et Lettres (PSL), Paris, France.

Corresponding author: anne-cecile.boulay@inserm.fr

Key-words: cortical development, cell density, cell distribution, blood vessel, astrocyte, oligodendrocyte, OPC.

Acknowledgments

We gratefully acknowledge the Orion technological core (IMACHEM-IBiSA) of Center for Interdisciplinary Research in Biology for their support, and especially Estelle Anceaume and Julien Dumont for assisting us with the Axio Zoom microscopy image acquisition. We thank the whole "physiology and physiopathology of the gliovascular unit" team for helpful comments and contribution on the VeCell plugin functionality.

Word count: 7453 words

Funding statement

This work was funded by Université PSL (Junior Fellow to ACB), ANR (ANR-23-CE16-0030 to ACB) and *the Fondation pour la Recherche Médicale* (EQU202303016292 to MCS). The "Physiology and Physiopathology of the Gliovascular Unit" research group at the Collège de France's CIRB is affiliated with PSL-NEURO and funded by Paris Sciences et Lettres (PSL) University.

32 **Table of Contents Entry**

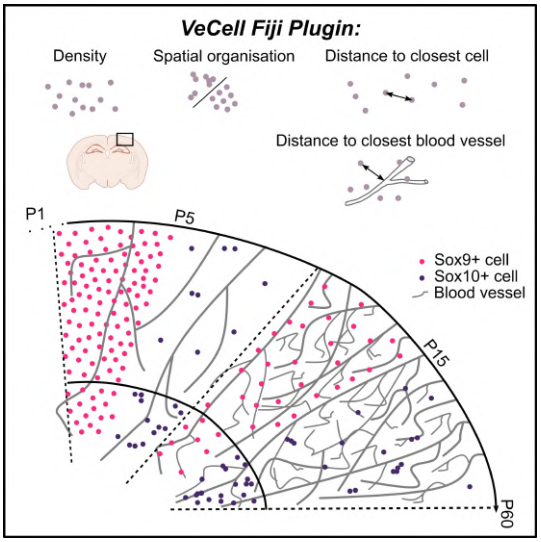

- VeCell: quantification of macroglial cell density, distribution, and proximity to blood vessels
- From P5, Sox9$^+$ cells are evenly distributed, unlike Sox10$^+$ cells
- From P15, Sox9$^+$ cells are located closer to blood vessels than Sox10$^+$ cells

Abstract

Brain cortical development results from the proliferation, differentiation, migration and maturation of many cell types. While neuronal development is well characterized, the mechanisms regulating macroglial cells (oligodendrocytes and astrocytes) development remain largely unknown. Recent works suggest that the vascular system plays a key, yet under-evaluated role in this process. To investigate this, we developed *VeCell*, a Fiji plugin designed to analyse the spatial organization of macroglial cells relative to blood vessels. Using immunolabeling for Sry-box transcription factor (Sox) 9 (macroglial progenitors and astrocytes) and Sox10 (oligodendrocyte lineage), we determined macroglia density, distribution and proximity to blood vessels from postnatal day (P) 1 to P60 in the somatosensory cortex. We showed that Sox9+ cells were evenly distributed across cortical layers with regular intercellular spacing. In contrast, Sox10+ cells concentrated in deeper cortical layers, and exhibited a random distribution. Vascular density and branching increased markedly between P5 and P15 and macroglial cells were closer to blood vessels from P15 onward. As a proof of concept, we used *Vecell* to show that astrocyte cortical distribution is preserved in MLC1-deficient mice, a model of Megalencephalic leukoencephalopathy with subcortical cysts, in which astrocyte perivascular coverage is altered. Thus, *VeCell* is a powerful tool to characterize and quantify macroglial cell distribution in the brain and in relation to the vasculature. It revealed distinct distribution and postnatal development patterns for astrocytes and oligodendrocytes.

Introduction

The mammalian cortex is a complex and highly organized tissue which contains diverse neuronal, glial and vascular cell types. Cortical development is driven by highly regulated and coordinated sequences of cell proliferation, differentiation and migration, and requires the fine tuning of production/elimination and attraction/repulsion mechanisms. Neurons and macroglial cells - astrocytes and oligodendrocytes - are generated from common multipotent neural precursor cells (NPCs) (Miller and Gauthier, 2007). After neuron production, which starts around embryonic day (E) 12 and peaks at E15, NPCs switch to gliogenesis around E18 to sequentially generate astrocyte progenitors and oligodendrocyte precursor cells (OPC). Cortical astrocytes are produced mainly during the first postnatal week from a combination of delaminating NPCs and local proliferation of astrocyte progenitors following colonization of the cortical parenchyma (Clavreul et al., 2019; Ge et al., 2012). From the second postnatal week, their migration is halted and astrocytes mature both molecularly and morphologically to finally tile the brain with non-overlapping domains (Bushong et al., 2004, 2002; Halassa et al., 2007). Oligodendrocyte lineage cells (OligoLC) comprise both oligodendrocyte precursors (OPCs) and myelinating oligodendrocytes (Foerster et al., 2024). During cortical development, OPCs are produced in three spatiotemporal waves. In the postnatal cortex, OPCs generated during the first embryonic wave undergo massive cell death. They are eliminated from the cerebral cortex by P10 and progressively replaced by OPCs locally-produced from cortical progenitors (Kessaris et al., 2006). After birth, OPCs progressively differentiate into oligodendrocytes (OLs) that form the myelin sheath around axons, mostly before the end of the 3rd postnatal week (Orduz et al., 2019), some NG2^{+} OPCs remaining in the mature brain.

Brain vascular network formation is initiated earlier than macroglial cells. Around embryonic day (E)9, the primary vascular network starts to form. From a perineural plexus, vascular sprouts invade the neuroectoderm by vasculogenesis and angiogenesis (Engelhardt, 2003). Postnatally, high angiogenesis rate results in an extensive vascular expansion between P8 and P12. New blood vessels (BVs) arising from ascending veins give rise to a dense capillary bed (Coelho-Santos and Shih, 2020).

BVs and macroglial cells interact during postnatal development. OPCs from ventral origin use blood vessels to migrate to the dorsal telencephalon during embryonic development (Lepiemme et al., 2022). Whether this also stands for postnatal cortical OPCs remains unknown. The role of BVs in astrocyte progenitor's migration is also unknown. A significant part of cortical Aldh1l1-positive cells, which include differentiated astrocytes as well as progenitors, are in contact with BVs at P1, but this population drops

at P5, in the middle of the highly proliferative and migratory phase of astrocyte progenitors (Clavreul et al., 2019; Freitas-Andrade et al., 2023). BVs have also been shown as a signalling source for both oligodendrocyte and astrocyte maturation (Paredes et al., 2021). A better characterization of how macroglial cells organize and relate to BV during the postnatal period is however necessary.

In this study, we developed *VeCell*, a new Fiji plugin to characterize macroglial cell density, distribution and distance to BVs in the developing and mature brain. Macroglial cells were immunolabelled for Sox 9 and 10 which regulate astrocyte and oligodendrocyte differentiation from glial precursors (Stolt and Wegner, 2010). Sox9 is expressed in NPCs and controls their switch to glial progenitors (Güven et al., 2020; Kang et al., 2012; Stolt, 2003). Its expression decreases during OligoLC specialisation, while increasing in astrocytes (Nagao et al., 2016; Klum et al., 2018). Sox10 is expressed in all OligoLCs, which are, during postnatal development, a mix of mature oligodendrocytes and OPCs originating either from cortical postnatal or ventral embryonic progenitors. In these cells, Sox10 regulates the transcription of myelin-forming genes (Foerster et al., 2024; Stolt et al., 2002).

Focusing on the somatosensory cortex, we found that Sox9+ cell density is homogeneous across cortical layers and peaks at P5, while Sox10+ cell density is maintained during postnatal development and is always higher in the deeper layers of the cortex. Sox9+ cells are distributed regularly within the parenchyma from P5. In contrast, Sox10+ cells are randomly distributed with varying distance between cells. Volume and branching of the cortical vascular network increase between P5 and P15. Sox9+ and Sox10+ cells become closer to BVs from P15. Absence of MLC1, an astrocyte protein enriched in perivascular processes does not alter astrocyte density and distribution.

111 **Materials and Methods**

112 *Animal experiments and ethical approval*

113 C57BL/6JRj, aged 5 to 60 days were purchased from Janvier labs (Le Genest-Saint-Isle, France) and
114 kept in pathogen-free conditions. All experiments and techniques complied with (i) the European
115 Directive 2010/63/EU on the protection of animals used for scientific purposes and (ii) the guidelines
116 issued by the French National Animal Care and Use Committee (reference: 2013/118). Animal cohorts
117 were made of males and females.

118 *Brain sections preparation*

119 Mice were sacrificed by cervical dislocation or decapitation depending on mouse age. Brains were
120 carefully collected and fixed in PBS/PFA 4% overnight at 4°C. After dehydration in 30% sucrose, brains
121 were cut into 80-µm-thick sections using a Leitz (1400) cryomicrotome and kept at -20°C in storage
122 solution (PBS/glycerol 30%/ethylene glycol 30%).

123 *Immunofluorescent staining*

124 Brain sections were rinsed three times 15 min in PBS and incubated in a blocking solution (BS) for 1h
125 at room temperature (RT). BS were PBS/normal goat serum 5%/Triton X-100 0.5% (Sox10) or
126 PBS/Triton X-100 0.5% (Sox9). Sections were incubated with primary antibodies diluted in the same BS
127 at 4°C overnight. After three rinses of 15 min in PBS, the sections were incubated for 2h at RT with
128 secondary antibodies and Hoechst reagent, rinsed in PBS, and mounted in Fluoromount G (Southern
129 Biotech, Birmingham, AL). Images were acquired using a wide-field Axio Zoom V16 microscope and its
130 Apotome V2 module (Zeiss) or spinning disk W1 (Nikon).

131 *Primary and secondary antibodies*

132 Primary antibodies used were polyclonal goat IgG anti-Sox9 (AF3075 Biotechne/R&D, 1:500),
133 monoclonal mouse/IgG2a anti-Sox10 (66786-1-Ig Proteintech, 1:500), AlexaF647-coupled Polyclonal
134 Goat IgG anti-Pecam-1/Cd31 (AF3628R-MTO, Biotechno, 1:300). Secondary antibodies used were
135 AlexaF555-coupled Goat anti-mouse IgG2a (A-21137 thermo Fisher, 1:1000) and AlexaF555-coupled
136 Donkey anti-Goat IgG (A-21432 thermo Fisher, 1:1000). Nuclei were stained using Hoechst (Thermo
137 fisher 62249, 1/2000).

138 *Image analysis*

139 Bins used to draw the ROI were defined based on cell density using nuclear staining Hoechst as
140 presented in Figure 1A. Bin 1 corresponds to the upper part of the cortex, Bin 2 to the deeper part. Layer
141 1 of the cortex was excluded because of its different organization and morphology of astrocytes.
142 The analysis was conducted in each region of interest using a custom-developed plugin called *VeCell*
143 (https://github.com/orion-cirb/VeCell) for the Fiji software (Schindelin et al., 2012). This plugin integrates
144 the Bio-Formats (Linkert et al., 2010), CLIJ (Haase et al., 2020) and 3D ImageJ Suite (Ollion et al., 2013)
145 libraries. VeCell consists in three analysis steps.
146 1) Macroglial cell detection in the Sox9/Sox10 channel: detection is performed using the 2D-stitched
147 version of the Cellpose algorithm (Stringer et al., 2021). A custom model was trained through the human-
148 in-the-loop workflow available in the Cellpose GUI. This model was initialized with the 'cyto2' pre-trained
149 Cellpose model and fine-tuned using a dataset of 36 images collected across three developmental
150 stages (P5, P15, and P60). Of these, 8 images were reserved for validation. The model was trained
151 using the following hyperparameters: learning rate = 0.1, weight decay = 0.0001, and number of epochs
152 = 500. Training and validation loss curves were monitored to ensure convergence. Model performance
153 was evaluated on a separate test set comprising 6 images (2 per developmental stage). The fine-tuned
154 model achieved a significant improvement in mean average precision (mAP) at an IoU threshold of 0.5,
155 increasing from 0.674 (for the 'cyto2' pretrained model) to 0.836. In addition, a separate model was
156 trained specifically for P1 developmental stage images to account for the more elongated cell
157 morphology and a lower signal-to-noise ratio. A dataset of 25 images was used for training, with 5
158 images reserved for validation. The P1-specific model was initialized from the 'cyto2' pretrained weights
159 and fine-tuned using similar hyperparameters: learning rate = 0.1, weight decay = 0.0001, and number
160 of epochs = 1000. Model performance was evaluated on a test set of 6 images, demonstrating a
161 substantial improvement in mAP at an IoU threshold of 0.5: from 0.539 for the 'cyto2' pretrained model
162 to 0.778 after fine-tuning. These models were deemed suitable for processing the entire dataset. During
163 inference, the following parameters were used: diameter = 20, flow threshold = 0.4, cell probability
164 threshold = 0.0, and stitching threshold = 0.5. Detected 3D cells were filtered based on volume to reduce
165 false positives. Only cells with a volume between 30 μm^3 and 3000 μm^3 were retained for downstream
166 analysis.
167 2) Blood vessel detection in the Pecam-1 channel: Images were normalized using the Quantile-Based
168 Normalization algorithm ("'Quantile Based Normalization' ImageJ PlugIn," n.d.) ensuring intensity

consistency across the dataset. A 3D median filter (*$radius_x$ = 4, $radius_y$ = 4, $radius_z$ = 1*) was applied to reduce noise while preserving vessel borders. Subsequently, a slice-by-slice 2D Difference of Gaussians filter *(σ_1 = 4, σ_2 = 8)* was applied to enhance vessel structures. A binary mask was generated using the Triangle automated thresholding method. The process was repeated with a second 2D Difference of Gaussians filter *(σ_1 = 7, σ_2 = 14)*, producing a second binary mask. These two binary masks were then merged using a maximum point operation to ensure comprehensive vessel detection. Postprocessing includes applying a 3D closing filter *($radius_x$ = 8, $radius_y$ = 8, $radius_z$ = 1)* to fill gaps in vessel structures, followed by a 3D median filter *($radius_x$ = 1, $radius_y$ = 1, $radius_z$ = 1)* to smooth vessel borders. The resulting binary mask was labelled in 3D to identify individual vessel structures, which are filtered by volume to retain only vessels exceeding 600 μm^3. Finally, the binary mask was skeletonized using CLIJ library, and branches shorter than 30 µm were excluded to ensure only meaningful segments were included in subsequent skeleton analysis.

<u>3) Computation and saving of metrics for macroglial cells and blood vessels.</u> For macroglial cells, were calculated: volume, distance to the nearest neighbor, mean and maximum distances to the 10 nearest neighbors, distance to the nearest vessel, and nearest vessel's diameter. Additionally, spatial statistical analysis was performed to identify clustering or dispersion patterns within the macroglial cell population. This was achieved using the 2D/3D Spatial Analysis Fiji plugin from the 3D ImageJ Suite library, which computes the distance function G. This function represents the cumulative distribution of distances between a typical point in the spatial pattern and its nearest neighbor (Andrey et al., 2010). The spatial distribution index (SDI) is derived from this analysis, serving as a metric to quantify the deviation of the observed spatial distribution from a completely random distribution. For BVs, skeleton analysis was conducted using the Analyze Skeleton Fiji plugin (Arganda-Carreras et al., 2010). The following metrics are obtained: total volume, total length, mean branch length, number of branches and junctions, mean diameter and diameter standard deviation.

Statistical analysis

Data shown on graphs are expressed as means and SD. Graphs and statistical analyses were performed using Graphpad Prism 8.0.2 software. For every data, we first verified that they followed a normal distribution using Shapirow-Wilk test. If not, we used Kruskal-Wallis and Mann-Whitney tests. If it is, we used a 2-way ANOVA followed by Sidak's multiple comparisons test to analyse differences between Bins or Tukey's multiple comparisons test, to analyse differences between ages. For SDI

199 distribution, comparison to normality was performed using Kolmogorov-Smirnov test. For percentages,
200 a chi-square test was used. Alpha thresholds for hypothesis verification were set at 0.05. Statistical tests
201 are indicated in the Figure legends and in the supplementary table 1.

202 *Use of Artificial Intelligence Generated Content*

203 ChatGPT (version 5) was used to perform the final editing of this manuscript, including grammar and
204 punctuation corrections, as well as improvements in clarity. It was not used to generate any content or
205 the original version of the text.

Results

Cortical density of macroglial cells during postnatal development

To characterize the postnatal development of cortical macroglial cells *in situ,* we immunolabelled brain sections from postnatal day (P) 1, P5, P15 and P60 for the transcription factors Sox9 and Sox10, focusing on the somatosensory cortex (Fig. 1A-D). Given previous studies showing different population dynamics across cortical layers (Orduz et al., 2019), we analysed the upper (Bin 1) and lower (Bin 2) parts of the cortex separately. Bins were determined by cell density revealed by nuclear labelling (Fig. 1B). Sox9+ and Sox10+ cell detection was automated using an adapted version of the *CellPose* deep learning-based algorithm and *Fiji* software (Schindelin et al., 2012; Stringer et al., 2021). Training on a set of 28 images collected at three developmental stages (P5, P15 and P60) allowed the detection of positive cells with 84% accuracy. At P1, immunolabelling was fainter and the nuclear shape was less circular than at later stages, requiring a specific training on 25 images. In this case, we obtained 78% of accuracy (Fig. 1E and Methods).

In the cortex, Sox9+ cells are predominantly glial progenitors at P1 and P5 and astrocytes from P15 (Fig. 1A). No difference was observed in Sox9+ cell density between the upper and lower cortical parts at any stage (Fig. 1B, C, F and Table S1). Density peaked at P5, with a significant increase between P1 and P5 followed by a significant decrease until P60. This decrease was particularly pronounced between P5 and P15 (Bin 1: 2.4-fold; P5: 1857±137; P15: 780±70.49; P60: 426.7±69.89 $10^2/mm^3$ cells; Bin 2: 2.3-fold; P5: 1816±181; P15: 775±34.66; P60: 359.7±110.8 $10^2/mm^3$ cells).

Sox10+ labelling was too faint to be analysed at P1. After P5, a small reduction in Sox10+ cell density was also observed in Bin 1 and after P15 in Bin 2 (Fig. 1G). A higher cell density was found in the lower part of the cortex (Bin 2), at all studied stages (Fig. 1B, D, G and Table S1).

We then compared the two cell populations. Sox9+ cells were more than 2 times more abundant than Sox10+ cells in the upper part of the cortex at P5. In the lower part, Sox9+ cells were more abundant at P5, but Sox10+ density was higher at P15 and P60 (Table S1).

Altogether, *VeCell* enables the detection of macroglial cells based on Sox9 and Sox10 nuclear immunolabelling. It reveals disparities in density between these two cell populations during cortical postnatal development.

Distribution of macroglial cells in the cerebral cortex during postnatal development

236 We next analysed the distribution of macroglial cells during postnatal development of the somato-
237 sensory cortex. First, we measured the mean distance between each cell and its nearest neighbour.
238 Consistent with the decreased cell density of Sox9+ cells after P5, the mean distance between
239 neighbouring Sox9+ cells progressively increased after P5 (Bin 1; P5: 12.6±0.2; P15: 17.1±0.2; P60:
240 22.5±1.4 µm) (Bin 2; P5: 13.0±0.5; P15: 18.0±0.5; P60: 25.6±0.9 µm). At P60, Sox9+ cells were also
241 slightly closer to each other in the upper compared to the lower part of the cortex (Fig. 2A). Measurement
242 of the mean distance between each Sox9+ cell and its 10 nearest Sox9+ cells gave similar results (Fig.
243 2B, Table S1). For Sox10+ cells, no difference in the mean distance between adjacent cells nor with 10
244 nearest cells was observed between P5 and P60 (Fig. 2C, D and Table S1). Consistent with density
245 differences (Fig. 1), Sox10+ cells were closer to each other in the lower part of the cortex from P5 (Fig.
246 2C, D and Table S1).
247 The spatial arrangement of cells within a population can vary from clustered to evenly spaced patterns,
248 which may reflect distinct developmental processes such as cellular attraction or repulsion. We used
249 the *Fiji* plugin "*2D/3D Spatial Analysis"* to assess the deviation from spatial randomness (Andrey et al.,
250 2010). We computed the G-function, the cumulative distribution function (CDF) of the distance between
251 a labelled cell and its nearest-neighbour. Shorter distances suggest clustering, while longer distances
252 indicate regular spacing (Fig. 2E). The experimental CDF was compared to the CDF of randomly
253 generated patterns within the same area and with the same number of cells. For each region of interest
254 (ROI), this comparison was computed as the Spatial Distribution Index (SDI) (Andrey et al., 2010).
255 Distribution of SDIs indicates the cell distribution pattern: uniformly distributed SDIs from 0 to 1 reflects
256 a random distribution of cells. SDIs near 0 suggest clustering. SDIs near 1 indicate regular spacing
257 (Andrey et al., 2010) (Fig. 2E).
258 Given the higher density of Sox10+ cells in the lower part of the cortex, we first focused our study on
259 this region. For Sox9+ cells, the SDIs distribution was significantly different from the random distribution
260 from P5 (Fig. 2F, Table S1), and values were not different from 1 (Bin 2: P5: 0.98±0.05; P15: 0.98±0.04;
261 P60: 0.88±0.3), revealing a regular distribution. At P1, however, SDIs were not different from normal
262 distribution, indicating a more random cell distribution. Same results were found in the upper layers of
263 the cortex (Table S1). These results indicated that, from P5 onwards, Sox9+ cells are regularly
264 organized.

265 For Sox10+ cells, the SDIs distribution differed between stages. At P5 and P15, distribution was
266 significantly different from random but not at P60 (Fig. 2G; Table S1). However, SDIs were always
267 significantly different from 1. The same result was found in the upper part of the cortex (Table S1). This
268 indicates that organisation of Sox10+ population always differs from a regular distribution and the mature
269 random distribution is established by P60.

270 Overall, our findings demonstrate that Sox9+ and Sox10+ cells follow distinct postnatal trajectories
271 adopting specific distribution patterns in the somatosensory cortex. Sox9+ cells maintain a regular
272 distribution from P5; Sox10+ cells are denser in deeper cortical layers, are never regularly organized
273 and change their spatial distribution during postnatal development.

274 **Distribution of glial cells relative to the vascular compartment**

275 Macroglial cells are closely associated with the brain vasculature. In the adult CNS, astrocytes entirely
276 cover the BVs through specialized processes called endfeet or perivascular astrocyte processes (PvAP)
277 (Cohen-Salmon et al., 2020). The formation of PvAPs, which occurs from birth to P15, plays a crucial
278 role in BV maturation (Cohen-Salmon et al., 2025; Freitas-Andrade et al., 2023; Gilbert et al., 2019,
279 2021; Mondo et al., 2020). Furthermore, parts of OPCs migrate along BVs during embryonic
280 development (Lepiemme et al., 2022).
281 To better understand the relationship between macroglial cells and BVs during postnatal development
282 we implemented *VeCell* with BV detection, immunolabeling endothelial cells for Pecam-1 (Fig. 3A, B).
283 The cortical vascular volume was normalized on the cortical volume and analysed at P1, P5, P15 and
284 P60. It changed during postnatal development: while stable between P1 and P5, a global increase in
285 vascular volume was observed between P5 and P15 (Fig. 3C) due to postnatal angiogenesis and
286 capillary bed extension (Coelho-Santos and Shih, 2020) (Bin 1; P5: 0.08±0.009; P15: 0.1±0.01 $\mu m^3/\mu m^3$)
287 (Bin 2; P5: 0.08±0.007; P15: 0.08±0.01 $\mu m^3/\mu m^3$). After P15, the vascular volume decreased, probably
288 related to the cortical growth (Fig. 3A, D and Table S1). Vessel branching followed the same trends (Fig.
289 3F and Table S1). Of note, the vascular volume and branching were globally slightly reduced in the
290 lower part of the cortex compared to the upper part but this difference was only significant at P15 for the
291 branching (Fig. 3D, E, F and Table S1).
292 We analysed the distance between macroglial cells and their nearest BV in the somatosensory cortex
293 at all stages (Fig. 4.A). We calculated both the mean distance to BVs for all cells (Fig. 4C and E) and

294 the percentage of cells with the nucleus directly apposed to BVs (Fig. 4D, F). The distance to BV was
295 the highest at P5, and similar for Sox9+ and Sox10+ cells (Fig. C-E, Table S1). In contrast, from P15,
296 Sox9+ cells were closer to BVs than Sox10+ cells and a higher proportion of Sox9+ were found apposed
297 to BV (Fig. 4B-D, Table S1).
298 Altogether, our approach allows to measure the distance between macroglial cells and BVs. We shows
299 that macroglial cells are more distant to BVs at P5. From P15, Sox9+ cells are closer to BVs than Sox10+
300 cells, suggesting distinct interactions between these macroglial populations and the vasculature. Thus,
301 we reveal different developmental changes in the spatial relationship between macroglial cells and BVs.
302
303 **Macroglial cell density and distribution are not altered in *Mlc1* KO cortex**
304 MLC1 is a membrane protein expressed by the astrocyte lineage in the brain whose absence leads to
305 Megalencephalic Leukoencephalopathy with subcortical Cysts (MLC), a rare type of leukodystrophy
306 (Passchier et al., 2024). MLC1 expression starts at P5. The protein progressively localizes within
307 astrocyte perivascular processes (PvAP) progressively and forms a junctional complex between PvAPs
308 with GlialCAM, which is mature around P15 (Gilbert et al., 2019; Teijido et al., 2007). In *Mlc1* KO mice,
309 the gliovascular interface is altered during development: astrocyte polarity and vascular coverage do
310 not develop properly and vascular functions are altered, including arteriolar contractility, CSF drainage
311 and neurovascular coupling (Gilbert et al., 2021). Thus, we hypothesized that absence of MLC1 could
312 also perturb astrocyte spatial arrangement.
313 On P60 somatosensory cortical sections, we observed no difference in the vascular volume and
314 branching (Fig. 4A-D). We found no difference in Sox9+ cell density (Fig. 4A and E). We observed
315 however a slight decrease in the distance between cells in *Mlc1* KO (Bin 1; *Mlc1* WT: 23.4±1.7; *Mlc1*
316 KO: 20.6±1.8 µm; Bin 2; *Mlc1* WT: 27.6±1.2; *Mlc1* KO: 23.7±1.6 µm). G-function-assessed distribution
317 pattern was similar between genotypes (Fig. 4H) and similar to our previous observation for Sox9+ cells:
318 SDI distribution different from the normal distribution and not different from 1 (Fig. 4G and Fig. 2). Finally,
319 the mean distance of Sox9+ cells to the closest BV was similar in *Mlc1* KO and controls (Fig. 4H).
320 We show that the vascular network as well as the distribution and density of Sox9+ cells, remain
321 unaffected in the absence of MLC1.
322
323
324

Discussion

Here we developed *VeCell*, a new Fiji plugin which allows the characterization of cell distribution. We focused our study on macroglial cells during postnatal development, based on the labelling of two transcription factors, Sox9 and Sox10, and of the vascular system.

Our approach first confirmed previously reported results regarding macroglia and vascular development. The density of Sox9+ cells was highest at P5 compared to P1 and P15/P60, similar to observations done with immunolabeling for Aldh1l1, an astrocyte-specific marker (Freitas-Andrade et al., 2023). We showed a higher density of Sox9+ cells compared to Sox10+ at P5 but not at P60, consistent with the reported intense proliferation of astrocyte progenitors around P4 (Clavreul et al., 2019) and the reduced expression of Sox9 in progenitors differentiating into OligoLC (Klum et al., 2018). We observed a smaller Sox10+ population in the upper part of the somatosensory cortex at all developmental stages, as previously described for OPCs (Ogino et al., 2020). This effect has been shown to rely on Reelin secreted by Cajal-retzius cells during late embryonic development, which acts as a driving force for OPC migration (Barber et al., 2022; Ogino et al., 2020). It is also consistent with the known higher density of myelinating oligodendrocytes in the lower cortical layers (Orduz et al., 2019). We observed a random distribution of Sox10+ cells within cortical layers as previously showed (Orduz et al., 2019). In contrast, we showed that Sox9+ density was identical between layers of the cortex and displayed a regular distribution indicating similar distances between cells. This is in line with the well-established organisation of astrocytes which occupy exclusive, non-overlapping domains that completely tile the cortical parenchyma in the mature brain, with each cell occupying a comparable volum (Bushong et al., 2004, 2002; Halassa et al., 2007). Using *Vecell* we could also reproduce previous results demonstrating the existence of a second wave of angiogenesis between P5 to and P15 (Coelho-Santos and Shih, 2020; Freitas-Andrade et al., 2023). To summarize, *VeCell* provides a fast and reliable tool to study macroglial distribution, vascular postnatal development, and their interrelationship. This approach can assist the gliovascular research community in accurately quantifying these parameters across different models and brain regions.

A key aspect of our study was the description of distinct patterns of distribution for macroglial cells. We found Sox9+ astrocytes to be regularly distributed within the parenchyma as early as P5, suggesting an extremely precise and coordinated colonization of the entire cortical parenchyma by macroglial progenitors/astrocytes. In contrast, Sox10+ cells were more randomly distributed. Astrocyte tiling of the

356 parenchyma is crucial to neuronal function (Baldwin et al., 2021). Such very early acquired organisation
357 suggests the presence of active mechanisms of active attraction and repulsion mechanisms between
358 astrocyte progenitors which remain to be fully understood. In contrast, Sox10+ cells displayed a random
359 distribution, suggesting different mechanisms orchestrating oligodendrocytes and OPCs postnatal
360 colonization of the cortical parenchyma.
361 The interaction between macroglial cells and BVs has gathered increasing interest in both
362 developmental and disease contexts (Lepiemme et al., 2022; Niu et al., 2019; Watkins et al., 2014). We
363 extended our plugin's functionality to calculate the distance between macroglial cells and BVs. Both
364 Sox9+ and Sox10+ cells were found to be closer to BVs at P15/P60 compared to P5. This result might
365 simply reflect the increased BVs density in the parenchyma. However, we cannot rule out the possibility
366 of active migration mechanism after P5, potentially driven by signals from vascular cells. At P1, Sox9+
367 cells were closer to BV compared to P5, despite a similar vascular network and an increased Sox9+ cell
368 density. This could, in contrast, indicate active mechanisms to repel Sox9+ cells from BVs or a transient
369 phase of cell migration along the vessels in the first days after birth as previously suggested (Freitas-
370 Andrade et al., 2023). Interestingly, Sox9+ nuclei were closer to BVs than Sox10+ which is consistent
371 with the known higher interaction between astrocytes and BVs, compared to oligodendrocytes, including
372 the complete coverage of BVs with PvAPs by P15 (Gilbert et al., 2021; Mathiisen et al., 2010).
373 To further assess the utility of *VeCell*, we analyzed a mouse model deficient for the astrocyte protein
374 MLC1, in which astrocyte polarity and PvAP formation are disrupted (Gilbert et al., 2021). We found no
375 difference in vascular organisation, consistent with our previous report (Gilbert et al., 2021). The regular
376 astrocyte spatial distribution was preserved. Thus, altered perivascular coverage does not necessarily
377 imply a change in astrocyte distribution. We cannot however exclude the possibility of transient
378 developmental changes as previously reported in this model (Gilbert et al., 2021). Beyond the study of
379 MLC, this analysis could be applied to identify defects in macroglial production and/or distribution in
380 various cerebrovascular and neurodevelopmental disorders that emerge during late brain development,
381 such as cavernomas, autoimmune diseases including multiple sclerosis and Neuromyelitis Optica,
382 arteriovenous malformations, muscular dystrophies affecting the brain, and other leukodystrophies
383 (Cohen-Salmon et al., 2025). While the destruction or abnormal proliferation of astrocytes,
384 oligodendrocytes, and OPCs have been frequently documented in diseases of the mature brain,

impairments in their production and spatial organization during postnatal development—whether or not related to the vascular system—remain largely unexplored

Altogether, we present a reliable, freely available Fiji plugin for analyzing macroglia organization using simple brain sections and low-resolution microscopy. This tool successfully reproduces previously reported findings, highlighting the robustness of our approach. Moreover, it revealed strong differences between the developmental trajectories of astrocyte and oligodendrocyte lineages. Notably, we observed that astrocytes adopt a remarkably regular distribution pattern that is established very early during postnatal development.

395 **Figure legends**
396
397 **Figure 1. Macroglial cells density during postnatal cortical development.**

398 **A.** Schematic representation of the studied area in the mouse brain (left) and developmental timeline
399 (right) of the macroglial cells expressing Sox9 (red) or Sox10 (magenta). **B.** Representative Axio Zoom
400 microscopy images of Hoechst (Blue), Sox9+ (red) or Sox10+ (magenta) showing the Region Of Interest
401 (ROI) within the somato-sensory cortex (Bin 1: upper layers, Bin 2: lower layers). **C,D.** Spinning disk W1
402 Z-stack projection images of Sox9+ (red) (C) or Sox10+ (magenta) (D) cells detected by
403 immunofluorescence at P5 and P60 in Bin 1 or Bin 2 of somatosensory cortical sections. **E**.
404 Representative Axio Zoom microscopy Z-stack projection image of Sox9+ cells detected by
405 immunofluorescence (top, white) on a P15 somatosensory cortical slice and the mask created by the
406 *VeCell* Fiji plugin (down, red). **F, G.** Analysis of the Sox9+ (F) and Sox10+ (G) cells densities shown as
407 a number of cells x10^2 per mm^3. N= 3 mice, n=1 section per animal, results are shown as mean of the
408 results on 4 ROI ± SD. Statistics: Mann Whitney test between ages (F) or between layers (G).
409

410 **Figure 2. Macroglial cells distribution during postnatal cortical development**

411 **A, B.** Analysis of mean distance to the closest (A) or 10 closest (B) Sox9+ cells, shown as the mean
412 distance for each cell of the studied area in the somato-sensory cortex. **C, D.** Analysis of mean distance
413 to the closest (A) or 10 closest (B) Sox10+ cells, shown as the mean distance for each cell of the studied
414 area in the somato-sensory cortex. **E**. Schematic summary of the G-function analysis of cell distribution.
415 Cells can follow three main behaviours: grouped (SDI=0), randomly distributed or regularly spaced
416 (SDI=1). The G-function is the cumulative distribution function (CDF) of the distance between a typical
417 point (the labelled cell) in the pattern and it nearest-neighbour. The experimental CDF (black curve) is
418 obtained for each ROI analysed and is compared to the CDF of randomly generated point patterns in
419 the same area and with the same number of points (red curve). For each ROI analysed, comparison
420 between the experimental and random CDF are computed as the Spatial Distribution Index (SDI).
421 Distribution of SDIs in each experimental condition indicates the distribution pattern followed by the cells.
422 **F**. Result of G-function analysis for Bin 2 Sox9+ (pink) and **G.** Sox10+ (purple) cells across postnatal
423 development. N= 3 mice, n=1 section per animal, results are shown as mean of the results on 4 ROI (A-
424 D) per section or the result of one ROI (F) ± SD. Statistics: Mann Whitney test between ages (A,B) or
425 layers (C,D). . F, G Kolmogorov-Smirnov test.

426

427 **Figure 3. Vascular system organisation during postnatal cortical development**

428 **A.** Representative Axio Zoom microscopy image of P1, P5, P15 and P60 somatosensory cortical section
429 stained for blood vessels (white) detected by immunofluorescence on Pecam-1. **B**. Representative Axio
430 Zoom microscopy Z stack projection image of P15 somatosensory cortical section stained for blood
431 vessels (white) detected by immunofluorescence on Pecam-1 with the superimposed masks created by
432 the VeCell Fiji plugin (in blue). i and ii are detailed of boxed area. i, BVs mask created by the VeCell Fiji
433 plugin (blue); ii, skeleton mask of the BV for branching analysis (green). **C**. Representative Axio Zoom
434 microscopy Z-stack projection images of P5 and P15 somatosensory cortical sections in Bin1, stained
435 for blood vessels detected by immunofluorescence for Pecam-1 (white). **D.** Analysis of the vascular
436 volume reported as BVs volume normalized by cortical volume. **E**. Representative Axio Zoom
437 microscopy Z-stack projection images of P15 somatosensory cortical sections Bin1 (left) or Bin2 (right),
438 stained for blood vessels detected by immunofluorescence for Pecam-1 (white). **F**. Analysis of the
439 vascular branching as the number of 10^3 branches per mm^3 of BVs. N= 3 mice, n=2 sections per animal.
440 Results are shown as mean of the results on 4 ROI per section ± SD. Statistics: 2-way ANOVA; p(age):
441 result of ANOVA for age effect; p(Bin): result of ANOVA for cortical layer effect.

442

443 **Figure 4. Macroglial cells distribution in relation to blood vessels during postnatal cortical**
444 **development**

445 **A.** Representative Axio Zoom microscopy Z-stack projection image of a P15 somatosensory cortical
446 section stained for blood vessels (white) detected by immunofluorescence on Pecam-1 with the
447 superimposed masks created by the VeCell Fiji plugin. BVs mask is in blue and Sox9+ cells are color
448 coded for their distance to nearest BV from magenta (close to BV) to yellow (far from BV). **i and ii** are
449 detailed of boxed area. i, immunofluorescence of Pecam-1-labeled BVs (white) and Sox9+ cells (red);
450 ii, BVs mask created by the VeCell Fiji plugin (blue) superimposed to the Pecam-1 staining (white) and
451 mask of Sox9+ cells color-coded for their distance to nearest BV. **B.** Representative Axio Zoom
452 microscopy Z-stack images of Sox9+ (red) or Sox10+ (magenta) cells and Pecam-1 (white) detected by
453 immunofluorescence at P1, P5, P15 and P60 in Bin 2 of somatosensory cortical sections. **C, E.** Analysis
454 of the mean distance to nearest BV of Sox9+ (C) and Sox10+ (E) cells. **D, F.** Analysis of the Sox9+ (D)
455 and Sox10+ (F) percentage of nuclei apposed to BV (distance to nearest BV=0 µm). N= 3 mice, n=1

456 section per animal. Results are shown as mean of the results on 4 ROI per section ± SD. Statistics:
457 Mann Whitney test between ages (C, E) and chi-square test between ages (D, F)
458
459 **Figure 5. Sox9+ cell density and distribution in the *Mlc1* KO model.**
460 **A.** Spinning disk W1 Z-stack projection images of P60 upper and lower parts of the somatosensory
461 cortex after immunostaining for Sox9 (red) and BV (grey). **B**. Masks created by the VeCell Fiji plugin on
462 P60 *Mlc1* KO Axio Zoom microscopy Z-stack projection image, BVs mask is in blue and Sox9+ cells are
463 color coded for their distance to nearest BV from magenta (close to BV) to yellow (far from BV). **C.**
464 Analysis of the vascular volume reported as BVs volume normalized by cortical volume. **D.** Analysis of
465 the vascular branching as the number of 10^3 branches per mm^3 of BVs. **E**. Analysis of the Sox9+ cells
466 densities shown as a number of cells $x10^2$ per mm^3. **F, G**. Analysis of mean distance to the closest (F)
467 or 10 closest (G) Sox9+ cells, shown as the mean distance for each cell of the studied area in the
468 somato-sensory cortex. H. Result of G-function analysis for Sox9+ cells in Bin 1 and 2 in the two
469 genotypes.
470 N= 3 WT and 4 *Mlc1* KO mice, n=3 section per animal, results are shown as mean of the results on 4
471 ROI per section ± SD. Statistics: C,D,E,F,G,I: 2-way ANOVA; $p_{(genotype)}$: result of ANOVA for genotype
472 effect; $p_{(Bin)}$: result of ANOVA for cortical layer effect. H: Kolmogorov-Smirnov test
473

References

Andrey, P., Kiêu, K., Kress, C., Lehmann, G., Tirichine, L., Liu, Z., Biot, E., Adenot, P.-G., Hue-Beauvais, C., Houba-Hérin, N., Duranthon, V., Devinoy, E., Beaujean, N., Gaudin, V., Maurin, Y., Debey, P., 2010. Statistical Analysis of 3D Images Detects Regular Spatial Distributions of Centromeres and Chromocenters in Animal and Plant Nuclei. PLOS Computational Biology 6, e1000853. https://doi.org/10.1371/journal.pcbi.1000853

Arganda-Carreras, I., Fernández-González, R., Muñoz-Barrutia, A., Ortiz-De-Solorzano, C., 2010. 3D reconstruction of histological sections: Application to mammary gland tissue. Microscopy Research and Technique 73, 1019–1029. https://doi.org/10.1002/jemt.20829

Baldwin, K.T., Tan, C.X., Strader, S.T., Jiang, C., Savage, J.T., Elorza-Vidal, X., Contreras, X., Rülicke, T., Hippenmeyer, S., Estévez, R., Ji, R.-R., Eroglu, C., 2021. HepaCAM controls astrocyte self-organization and coupling. Neuron 109, 2427-2442.e10. https://doi.org/10.1016/j.neuron.2021.05.025

Barber, H.M., Ali, M.F., Kucenas, S., 2022. Glial Patchwork: Oligodendrocyte Progenitor Cells and Astrocytes Blanket the Central Nervous System. Front. Cell. Neurosci. 15. https://doi.org/10.3389/fncel.2021.803057

Bushong, E.A., Martone, M.E., Ellisman, M.H., 2004. Maturation of astrocyte morphology and the establishment of astrocyte domains during postnatal hippocampal development. International Journal of Developmental Neuroscience 22, 73–86. https://doi.org/10.1016/j.ijdevneu.2003.12.008

Bushong, E.A., Martone, M.E., Jones, Y.Z., Ellisman, M.H., 2002. Protoplasmic astrocytes in CA1 stratum radiatum occupy separate anatomical domains. The Journal of neuroscience 22, 183–192.

Clavreul, S., Abdeladim, L., Hernández-Garzón, E., Niculescu, D., Durand, J., Ieng, S.-H., Barry, R., Bonvento, G., Beaurepaire, E., Livet, J., Loulier, K., 2019. Cortical astrocytes develop in a plastic manner at both clonal and cellular levels. Nature Communications 10, 4884. https://doi.org/10.1038/s41467-019-12791-5

Coelho-Santos, V., Shih, A.Y., 2020. Postnatal development of cerebrovascular structure and the neurogliovascular unit. WIREs Developmental Biology 9, e363. https://doi.org/10.1002/wdev.363

Cohen-Salmon, M., Guille, N., Boulay, A.-C., 2025. Development of perivascular astrocyte processes. Front. Neurosci. 19. https://doi.org/10.3389/fnins.2025.1585340

Cohen-Salmon, M., Slaoui, L., Mazaré, N., Gilbert, A., Oudart, M., Alvear-Perez, R., Elorza-Vidal, X., Chever, O., Boulay, A.-C., 2020. Astrocytes in the regulation of cerebrovascular functions. Glia. https://doi.org/10.1002/glia.23924

Engelhardt, B., 2003. Development of the blood-brain barrier. Cell Tissue Res 314, 119–129. https://doi.org/10.1007/s00441-003-0751-z

Foerster, S., Floriddia, E.M., van Bruggen, D., Kukanja, P., Hervé, B., Cheng, S., Kim, E., Phillips, B.U., Heath, C.J., Tripathi, R.B., Call, C., Bartels, T., Ridley, K., Neumann, B., López-Cruz, L., Crawford, A.H., Lynch, C.J., Serrano, M., Saksida, L., Rowitch, D.H., Möbius, W., Nave, K.-A., Rasband, M.N., Bergles, D.E., Kessaris, N., Richardson, W.D., Bussey, T.J., Zhao, C., Castelo-Branco, G., Franklin, R.J.M., 2024. Developmental origin of oligodendrocytes determines their function in the adult brain. Nat Neurosci 27, 1545–1554. https://doi.org/10.1038/s41593-024-01666-8

Freitas-Andrade, M., Comin, C.H., Van Dyken, P., Ouellette, J., Raman-Nair, J., Blakeley, N., Liu, Q.Y., Leclerc, S., Pan, Y., Liu, Z., Carrier, M., Thakur, K., Savard, A., Rurak, G.M., Tremblay, M.-È., Salmaso, N., da F. Costa, L., Coppola, G., Lacoste, B., 2023. Astroglial Hmgb1 regulates postnatal astrocyte morphogenesis and cerebrovascular maturation. Nat Commun 14, 4965. https://doi.org/10.1038/s41467-023-40682-3

Ge, W.-P., Miyawaki, A., Gage, F.H., Jan, Y.N., Jan, L.Y., 2012. Local generation of glia is a major astrocyte source in postnatal cortex. Nature 484, 376–380. https://doi.org/10.1038/nature10959

Gilbert, A., Elorza-Vidal, X., Rancillac, A., Chagnot, A., Yetim, M., Hingot, V., Deffieux, T., Boulay, A.-C., Alvear-Perez, R., Cisternino, S., Martin, S., Taib, S., Gelot, A., Mignon, V., Favier, M., Brunet, I., Declèves, X., Tanter, M., Estevez, R., Vivien, D., Saubaméa, B., Cohen-Salmon, M., 2021. Megalencephalic leukoencephalopathy with subcortical cysts is a developmental disorder of the gliovascular unit.

Gilbert, A., Vidal, X.E., Estevez, R., Cohen-Salmon, M., Boulay, A.-C., 2019. Postnatal development of the astrocyte perivascular MLC1/GlialCAM complex defines a temporal window for the gliovascular unit maturation. Brain Struct Funct 224, 1267–1278. https://doi.org/10.1007/s00429-019-01832-w

Güven, A., Kalebic, N., Long, K.R., Florio, M., Vaid, S., Brandl, H., Stenzel, D., Huttner, W.B., 2020. Extracellular matrix-inducing Sox9 promotes both basal progenitor proliferation and gliogenesis in developing neocortex [WWW Document]. eLife. https://doi.org/10.7554/eLife.49808

Haase, R., Royer, L.A., Steinbach, P., Schmidt, D., Dibrov, A., Schmidt, U., Weigert, M., Maghelli, N., Tomancak, P., Jug, F., Myers, E.W., 2020. CLIJ: GPU-accelerated image processing for everyone. Nat Methods 17, 5–6. https://doi.org/10.1038/s41592-019-0650-1

Halassa, M.M., Fellin, T., Takano, H., Dong, J.-H., Haydon, P.G., 2007. Synaptic Islands Defined by the Territory of a Single Astrocyte. J. Neurosci. 27, 6473–6477. https://doi.org/10.1523/JNEUROSCI.1419-07.2007

Kang, P., Lee, H.K., Glasgow, S.M., Finley, M., Donti, T., Gaber, Z.B., Graham, B.H., Foster, A.E., Novitch, B.G., Gronostajski, R.M., Deneen, B., 2012. Sox9 and NFIA Coordinate a Transcriptional Regulatory Cascade during the Initiation of Gliogenesis. Neuron 74, 79–94. https://doi.org/10.1016/j.neuron.2012.01.024

Kessaris, N., Fogarty, M., Iannarelli, P., Grist, M., Wegner, M., Richardson, W.D., 2006. Competing waves of oligodendrocytes in the forebrain and postnatal elimination of an embryonic lineage. Nat Neurosci 9, 173–179. https://doi.org/10.1038/nn1620

Klum, S., Zaouter, C., Alekseenko, Z., Björklund, Å.K., Hagey, D.W., Ericson, J., Muhr, J., Bergsland, M., 2018. Sequentially acting SOX proteins orchestrate astrocyte- and oligodendrocyte-specific gene expression. EMBO reports 19, e46635. https://doi.org/10.15252/embr.201846635

Lepiemme, F., Stoufflet, J., Javier-Torrent, M., Mazzucchelli, G., Silva, C.G., Nguyen, L., 2022. Oligodendrocyte precursors guide interneuron migration by unidirectional contact repulsion. Science 376, eabn6204. https://doi.org/10.1126/science.abn6204

Linkert, M., Rueden, C.T., Allan, C., Burel, J.-M., Moore, W., Patterson, A., Loranger, B., Moore, J., Neves, C., MacDonald, D., Tarkowska, A., Sticco, C., Hill, E., Rossner, M., Eliceiri, K.W., Swedlow, J.R., 2010. Metadata matters: access to image data in the real world. Journal of Cell Biology 189, 777–782. https://doi.org/10.1083/jcb.201004104

Mathiisen, T.M., Lehre, K.P., Danbolt, N.C., Ottersen, O.P., 2010. The perivascular astroglial sheath provides a complete covering of the brain microvessels: an electron microscopic 3D reconstruction. Glia 58, 1094–1103. https://doi.org/10.1002/glia.20990

Miller, F.D., Gauthier, A.S., 2007. Timing Is Everything: Making Neurons versus Glia in the Developing Cortex. Neuron 54, 357–369. https://doi.org/10.1016/j.neuron.2007.04.019

Mondo, E., Becker, S.C., Kautzman, A.G., Schifferer, M., Baer, C.E., Chen, J., Huang, E.J., Simons, M., Schafer, D.P., 2020. A Developmental Analysis of Juxtavascular Microglia Dynamics and Interactions with the Vasculature. J Neurosci 40, 6503–6521. https://doi.org/10.1523/JNEUROSCI.3006-19.2020

Nagao, M., Ogata, T., Sawada, Y., Gotoh, Y., 2016. Zbtb20 promotes astrocytogenesis during neocortical development. Nat Commun 7, 11102. https://doi.org/10.1038/ncomms11102

Niu, J., Tsai, H.-H., Hoi, K.K., Huang, N., Yu, G., Kim, K., Baranzini, S.E., Xiao, L., Chan, J.R., Fancy, S.P.J., 2019. Aberrant oligodendroglial-vascular interactions disrupt the Blood Brain Barrier triggering CNS inflammation. Nat Neurosci 22, 709–718. https://doi.org/10.1038/s41593-019-0369-4

Ogino, H., Nakajima, T., Hirota, Y., Toriuchi, K., Aoyama, M., Nakajima, K., Hattori, M., 2020. The Secreted Glycoprotein Reelin Suppresses the Proliferation and Regulates the Distribution of Oligodendrocyte Progenitor Cells in the Embryonic Neocortex. J. Neurosci. 40, 7625–7636. https://doi.org/10.1523/JNEUROSCI.0125-20.2020

Ollion, J., Cochennec, J., Loll, F., Escudé, C., Boudier, T., 2013. TANGO: a generic tool for high-throughput 3D image analysis for studying nuclear organization. Bioinformatics 29, 1840–1841. https://doi.org/10.1093/bioinformatics/btt276

Orduz, D., Benamer, N., Ortolani, D., Coppola, E., Vigier, L., Pierani, A., Angulo, M.C., 2019. Developmental cell death regulates lineage-related interneuron-oligodendroglia functional clusters and oligodendrocyte homeostasis. Nat Commun 10, 4249. https://doi.org/10.1038/s41467-019-11904-4

Paredes, I., Vieira, J.R., Shah, B., Ramunno, C.F., Dyckow, J., Adler, H., Richter, M., Schermann, G., Giannakouri, E., Schirmer, L., Augustin, H.G., Ruiz de Almodóvar, C., 2021. Oligodendrocyte precursor cell specification is regulated by bidirectional neural progenitor–endothelial cell crosstalk. Nat Neurosci 24, 478–488. https://doi.org/10.1038/s41593-020-00788-z

Passchier, E.M.J., Bisseling, Q., Helman, G., van Spaendonk, R.M.L., Simons, C., Olsthoorn, R.C.L., van der Veen, H., Abbink, T.E.M., van der Knaap, M.S., Min, R., 2024. Megalencephalic leukoencephalopathy with subcortical cysts: a variant update and review of the literature. Front Genet 15, 1352947. https://doi.org/10.3389/fgene.2024.1352947

"Quantile Based Normalization" ImageJ PlugIn [WWW Document], n.d. URL https://www.longair.net/edinburgh/imagej/quantile-normalization/ (accessed 12.10.24).

Schindelin, J., Arganda-Carreras, I., Frise, E., Kaynig, V., Longair, M., Pietzsch, T., Preibisch, S., Rueden, C., Saalfeld, S., Schmid, B., Tinevez, J.-Y., White, D.J., Hartenstein, V., Eliceiri, K., Tomancak, P., Cardona,

A., 2012. Fiji: an open-source platform for biological-image analysis. Nat Methods 9, 676–682. https://doi.org/10.1038/nmeth.2019

Stolt, C.C., 2003. The Sox9 transcription factor determines glial fate choice in the developing spinal cord. Genes & Development 17, 1677–1689. https://doi.org/10.1101/gad.259003

Stolt, C.C., Rehberg, S., Ader, M., Lommes, P., Riethmacher, D., Schachner, M., Bartsch, U., Wegner, M., 2002. Terminal differentiation of myelin-forming oligodendrocytes depends on the transcription factor Sox10. Genes Dev. 16, 165–170. https://doi.org/10.1101/gad.215802

Stolt, C.C., Wegner, M., 2010. SoxE function in vertebrate nervous system development. The International Journal of Biochemistry & Cell Biology, SOX Transcription Factors 42, 437–440. https://doi.org/10.1016/j.biocel.2009.07.014

Stringer, C., Wang, T., Michaelos, M., Pachitariu, M., 2021. Cellpose: a generalist algorithm for cellular segmentation. Nat Methods 18, 100–106. https://doi.org/10.1038/s41592-020-01018-x

Teijido, O., Casaroli-Marano, R., Kharkovets, T., Aguado, F., Zorzano, A., Palacín, M., Soriano, E., Martínez, A., Estévez, R., 2007. Expression patterns of MLC1 protein in the central and peripheral nervous systems. Neurobiology of Disease 26, 532–545. https://doi.org/10.1016/j.nbd.2007.01.016

Watkins, S., Robel, S., Kimbrough, I.F., Robert, S.M., Ellis-Davies, G., Sontheimer, H., 2014. Disruption of astrocyte–vascular coupling and the blood–brain barrier by invading glioma cells. Nat Commun 5, 4196. https://doi.org/10.1038/ncomms5196

Figure 1

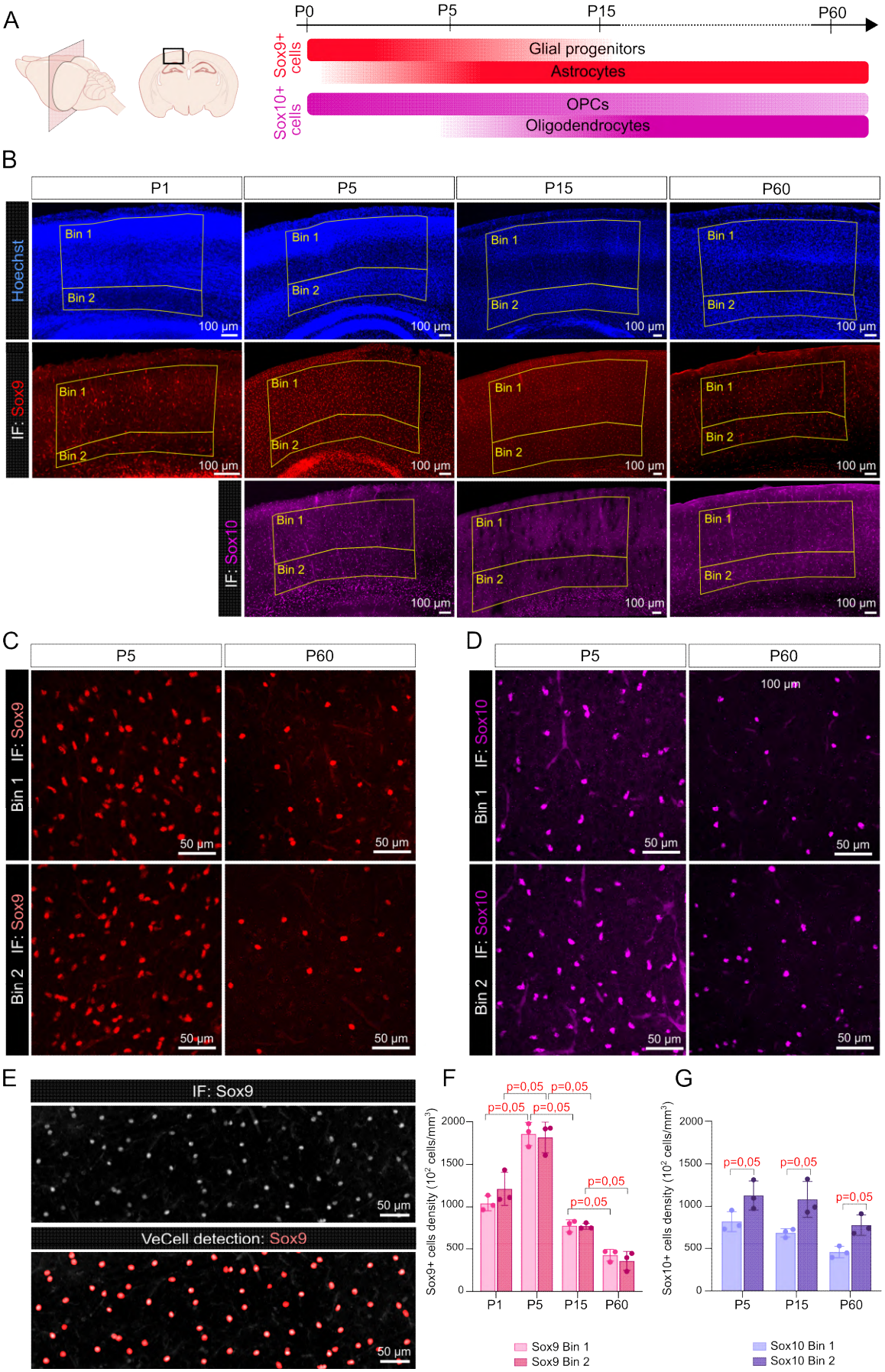
A
P0
P5
P15
P60
Sox9+ cells
Glial progenitors
Astrocytes
Sox10+ cells
OPCs
Oligodendrocytes
B
P1
P5
P15
P60
Hoechst
IF: Sox9
IF: Sox10
Bin 1
Bin 2
100 µm
C
P5
P60
Bin 1 IF: Sox9
Bin 2 IF: Sox9
50 µm
D
Bin 1 IF: Sox10
Bin 2 IF: Sox10
E
IF: Sox9
VeCell detection: Sox9
F
Sox9+ cells density (10² cells/mm³)
p=0,05
Sox9 Bin 1
Sox9 Bin 2
G
Sox10+ cells density (10² cells/mm³)
Sox10 Bin 1
Sox10 Bin 2

606

Figure 2

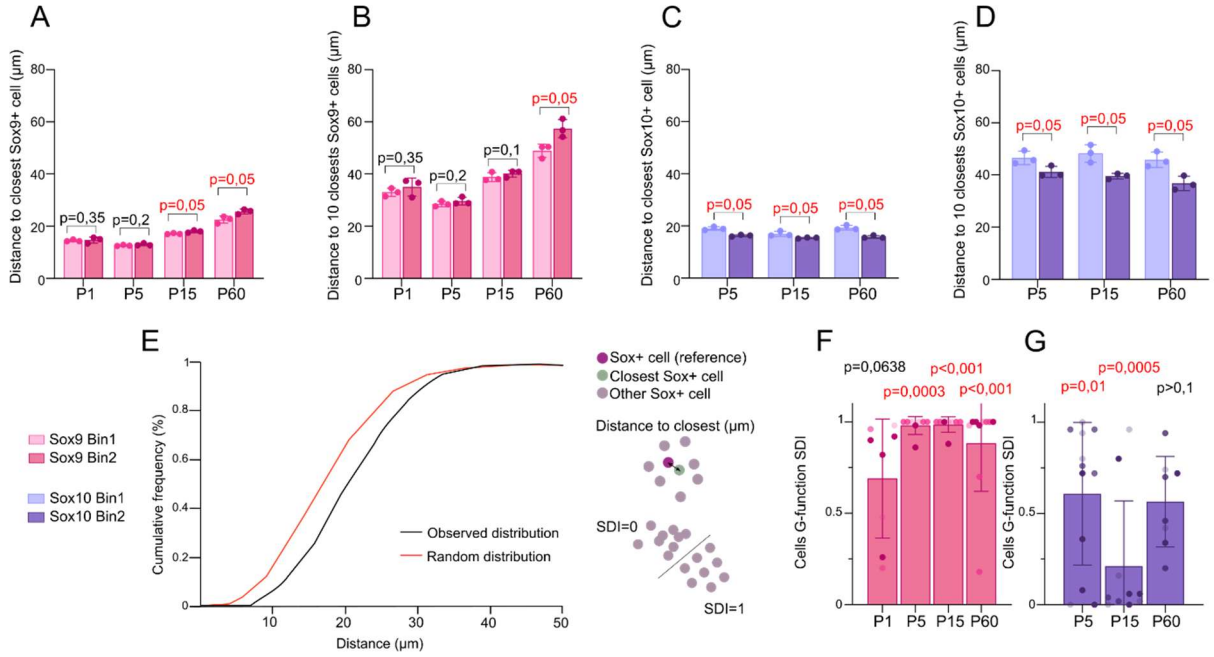
A
Distance to closest Sox9+ cell (µm)
p=0,35
p=0,2
p=0,05
p=0,05
P1
P5
P15
P60
B
Distance to 10 closests Sox9+ cells (µm)
p=0,35
p=0,2
p=0,1
p=0,05
C
Distance to closest Sox10+ cell (µm)
p=0,05
p=0,05
p=0,05
D
Distance to 10 closests Sox10+ cells (µm)
p=0,05
p=0,05
p=0,05
E
Sox9 Bin1
Sox9 Bin2
Sox10 Bin1
Sox10 Bin2
Cumulative frequency (%)
Observed distribution
Random distribution
Distance (µm)
Sox+ cell (reference)
Closest Sox+ cell
Other Sox+ cell
Distance to closest (µm)
SDI=0
SDI=1
F
p=0,0638
p<0,001
p=0,0003
p<0,001
Cells G-function SDI
G
p=0,0005
p=0,01
p>0,1

607

Figure 3

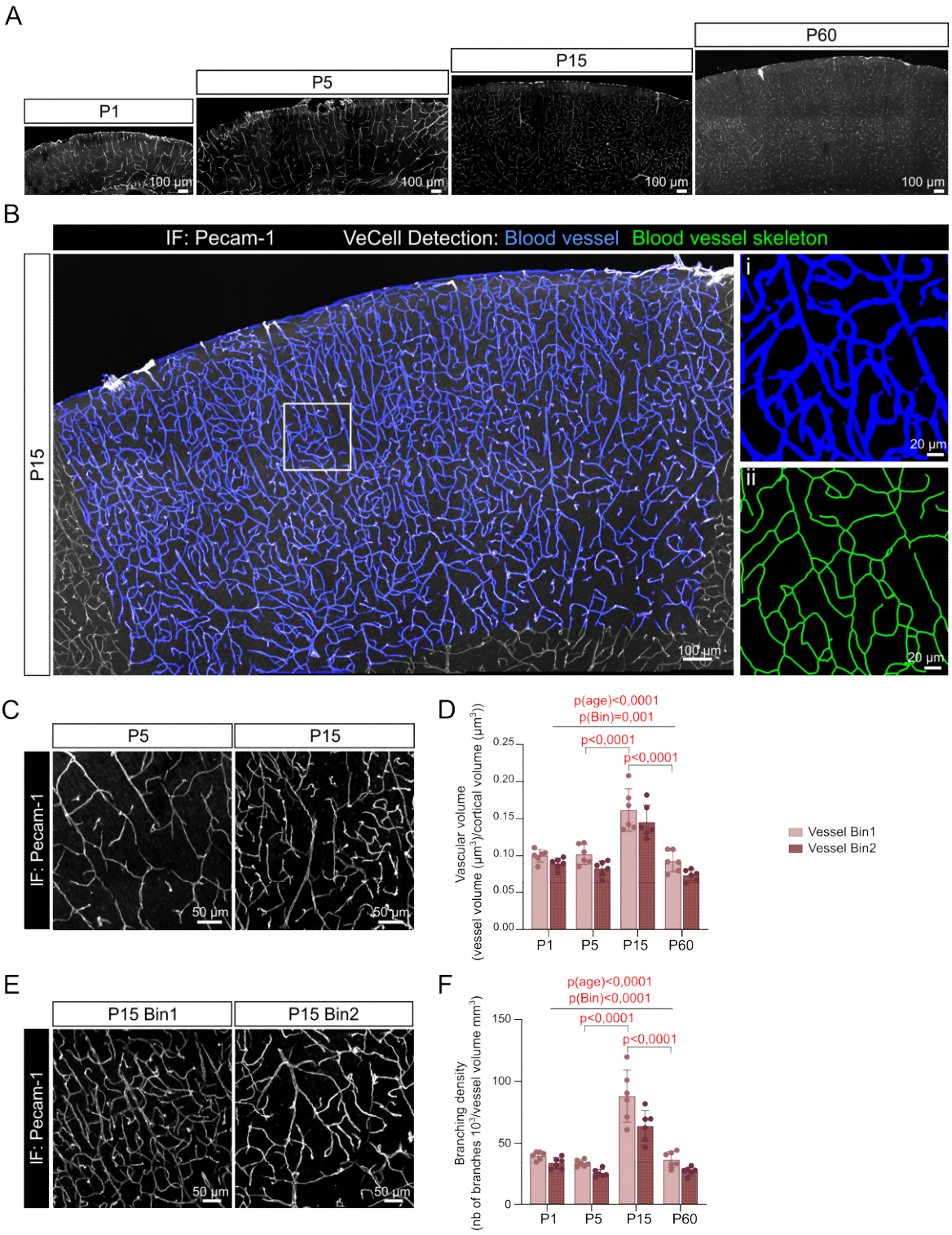
A
P1
P5
P15
P60
100 µm
B
IF: Pecam-1
VeCell Detection: Blood vessel Blood vessel skeleton
P15
100 µm
i
20 µm
ii
20 µm
C
P5
P15
IF: Pecam-1
50 µm
D
p(age)<0,0001
p(Bin)=0,001
p<0,0001
p<0,0001
Vascular volume
(vessel volume (µm³)/cortical volume (µm³))
0.25
0.20
0.15
0.10
0.05
0.00
P1
P5
P15
P60
Vessel Bin1
Vessel Bin2
E
P15 Bin1
P15 Bin2
IF: Pecam-1
50 µm
F
p(age)<0,0001
p(Bin)<0,0001
p<0,0001
p<0,0001
Branching density
(nb of branches 10³/vessel volume mm³)
150
100
50
0
P1
P5
P15
P60

608

Figure 4

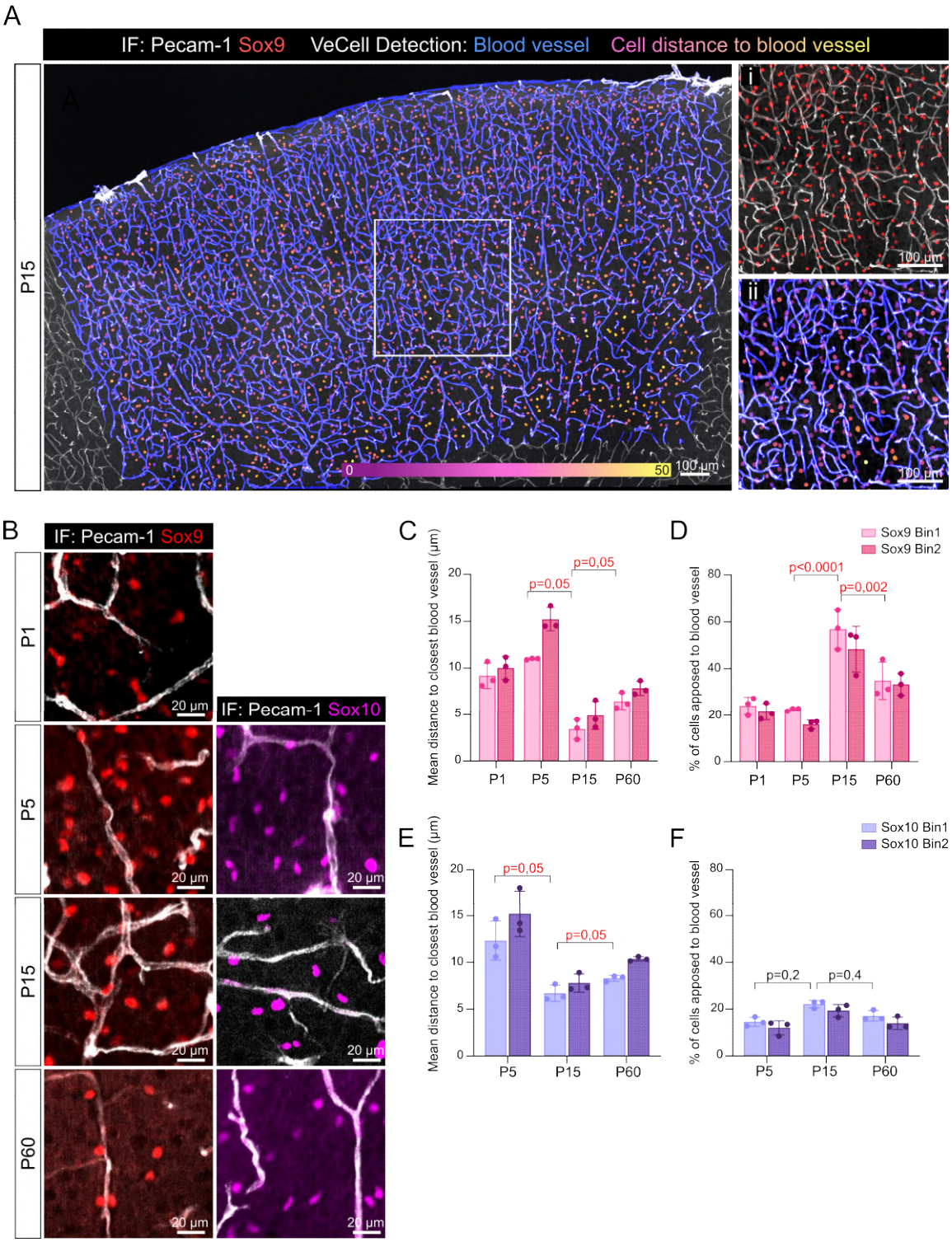

609

610

Figure 5

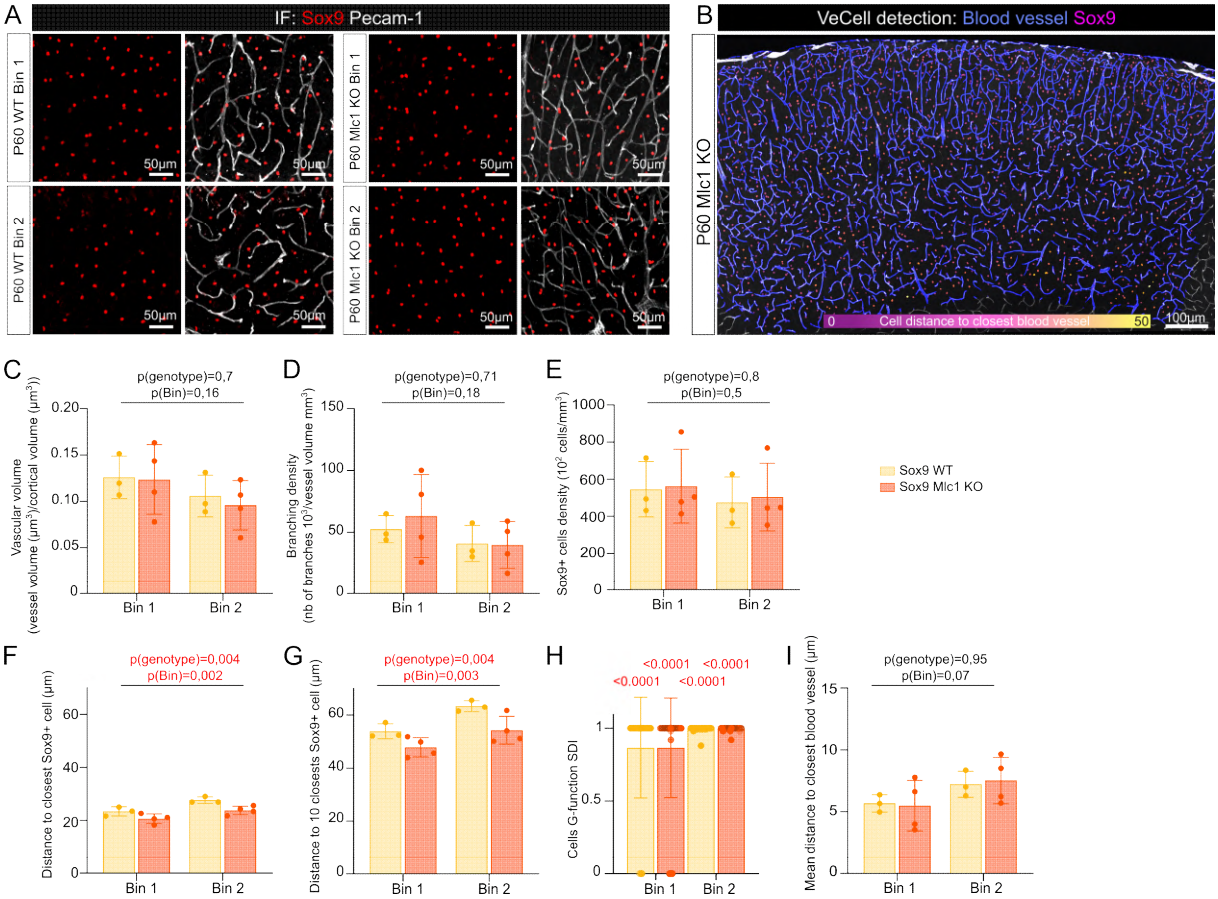
A
IF: Sox9 Pecam-1
P60 WT Bin 1
P60 WT Bin 2
P60 Mlc1 KO Bin 1
P60 Mlc1 KO Bin 2
50µm
B
VeCell detection: Blood vessel Sox9
P60 Mlc1 KO
0
Cell distance to closest blood vessel
50
100µm
C
p(genotype)=0,7
p(Bin)=0,16
Vascular volume
(vessel volume (µm³)/cortical volume (µm³))
D
p(genotype)=0,71
p(Bin)=0,18
Branching density
(nb of branches 10³/vessel volume mm³)
E
p(genotype)=0,8
p(Bin)=0,5
Sox9+ cells density (10² cells/mm³)
Sox9 WT
Sox9 Mlc1 KO
F
p(genotype)=0,004
p(Bin)=0,002
Distance to closest Sox9+ cell (µm)
G
p(genotype)=0,004
p(Bin)=0,003
Distance to 10 closests Sox9+ cell (µm)
H
<0.0001
<0.0001
<0.0001
<0.0001
Cells G-function SDI
I
p(genotype)=0,95
p(Bin)=0,07
Mean distance to closest blood vessel (µm)
Bin 1
Bin 2

611